Title

Permeability variations within mining-induced fractured rock mass and its influence on groundwater inrush

Journal

Environmental Earth Sciences, 75(4)

ISSN

1866-6280

Authors

Wang, WX
Sui, WH
Faybishenko, B
et al.

Publication Date

2016-02-01

DOI

10.1007/s12665-015-5064-5

Peer reviewed

Permeability variations within mining-induced fractured rock mass and its influence on groundwater inrush

W. X. Wang[1,2,4] • W. H. Sui[1] • B. Faybishenko[3] • W. T. Stringfellow[3,4]

[1] State Key Laboratory for Geomechanics and Deep Underground Engineering, School of Resources and Geosciences, China University of Mining and Technology, Xuzhou 221008, China [2] Henan Province Key Laboratory of Rock and Soil Mechanics and Structural Engineering, North China University of Water Resources and Electric Power, Zhengzhou 450045, China [3] Earth Sciences Division, Lawrence Berkeley National Laboratory, Berkeley, CA, USA [4] Ecological Engineering Research Program, School of Engineering and Computer Science, University of the Pacific, Stockton, CA, USA

W. H. Sui suiwanghua@cumt.edu.cn; W. X. Wang wang603698305@163.com; B. Faybishenko bafaybishenko@lbl.gov; W. T. Stringfellow wstringfellow@pacific.edu

Abstract

This paper is concerned with the evaluation of permeability of fractured rock mass due to the cover stress re-establishment, which is a major factor in controlling water and gas flow rate induced by mining operations in fractured rock. The case study considered in this paper is based on the results of observations of groundwater inrush and a decrease in water inflow from the fractured roof strata due to mining advancing in the Taiping Coalmine, Shandong Province, China. A conceptual model of an effective porous media was used to assess the permeability distribution in the fractured zone induced by coal mining. The cover stress re-establishment in gob fractured rock mass was evaluated using an empirical formula based on the surface subsidence. A simplified conceptual model of the fractured zone was used to evaluate the deformation of fractured zone along with the evaluation of changes in the rock permeability above the gob due to the cover stress re-establishment. These data were then used to calculate the water inflow rate into the panel. Predicted water inflow rates have been found to be in good agreement with those from monitoring data. This study improved the understanding of the mechanisms of the post-mining cover stress re-establishment on permeability change of the overburden fracture rock strata. These results can then be applied for numerical simulations of the process of overburden failure and consequent groundwater inrush due to coal mining.

Keywords: Underground coal mining, Gob, Bulking factor, Permeability of fractured rock mass, Cover stress re-establishment, Groundwater inrush rate

Introduction

Many underground coal mines are threatened by rivers, lakes, reservoirs or groundwater during coal extraction (Niskovskiy and Vasianovich 1996; Zhang and Shen 2004; Sun et al. 2008; Zhang et al. 2010; Li et al. 2013).

When the coal seam is excavated, the overburden strata are disturbed in order of severity and can be divided into caving, fractured and continuous deformation zones from the immediate roof toward the surface (Peng and Chiang 1984). The fractures may propagate upward to the upper strata, resulting in a dramatic increase in rock permeability (Das 2000). If these fractures reach the water bodies above the coal seam, rapid water influx, quicksand or flooding accidents may occur (Zhang and Shen 2004; Zhang et al. 2010; Li et al. 2013).

The water flow fractured zone (WFFZ), which includes caving and fractured zones (Sui et al. 2015) is the main pathway for water inrush. Most of the previous studies focused on the post-mining investigation of the WFFZ to determine whether or not the water inrush occured. Many empirical formulas about the mining thickness and the maximum height of WFFZ have been proposed based on in situ measurements, laboratory physical experiments, numerical modeling and mathematical approaches, providing the basis for predicting of a maximum height of the WFFZ for coal mines with similar hydrogeological and engineering geological conditions (Singh and Kendorski 1981; Chuen 1979; Fawcett et al. 1986; Majdi et al. 2012).

When the water inrush occurs, the permeability evolution at the water rush beginning sites in the WFFZ primarily defines the flowing rate. Stress relief is the primary reason for the permeability increase in the overburden. The post-mining hydraulic conductivity increases gradually to maximum then decreases to a certain value. The enhancement of the horizontal component of rock permeability is usually much larger than that in the vertical direction, although the vertical component of the rock permeability dominates the water flow (Zhang and Shen 2004). Liu and Elsworth (1997) evaluated the three-dimensional hydraulic conductivity field accompanying underground coal mining by a longwall panel, and the model results showed that hydraulic conductivity in shallow depths ahead of the advancing face and in deep zones behind the face increased, particularly in the caving and abutment shear zone. Schatzel et al. (2012) proposed that the draping effect in the tensional zone of the overburden and the coal matrix shrinkage are the two mechanisms causing the increase in fracture permeability during overburden compaction via borehole monitoring. Karacan and Goodman (2009) investigated the relationship between the permeability and the overburden depth, as well as the locations of the borehole and the mining face advancing rates, the results showed that high permeability fractures developed less in stiff and thick roof, greater overburden depths generally caused earlier fracturing with lower permeability, and increasing mining rates generally resulted in lower permeability in the overburden. Kim et al. (1997) proposed a finite element poroelastic model to evaluate fully coupled strata deformation and groundwater flow resulting from underground longwall mining in variably saturated fractured geologic media using an equivalent porous elastic continuum representation.

The stress distribution around the longwall mining panels showed that the stress in the mining-induced fractured rock mass re-established as the mining distance increased (Li et al. 1992; Singh et al. 1995; Yavuz 2004; Shabanimashcool and Li 2012). In situ monitoring results showed that the water table of the aquifer decreased at first and then rose gradually as the mining distance increased, which predicted that the permeability in the fractured zone decreased due to stress re-establishment (Zhang and Shen 2004; Zhang et al. 2006, 2010; Wang et al. 2014). Karacan et al. (2007) estimated that the initial permeability of caving zone was 1×10^{-6} m^2, but as the mining advanced, the rock fragments in the caving zone began to support the vertical stress from the upper strata. It is impossible for the fractured rock mass to revert to its original intact state, but the voids volume and permeability decreased when the stress increased. Ren et al. (1997) estimated that permeability was 1×10^{-10} m^2 in the compression area of the gob. Zhang et al. (2010) proposed that under the gravitational force of overlying layers, the structural fractures in the severely weathered rock were closed under compression; the porosity and permeability of the severely weathered rock decrease, resulting in the loss of rock ability to retain water, so that the severely weathered rock layer becomes an aquifuge. The open fractures with small aperture in the upper parts of the WFFZ become closed after stress re-establishment, while those with big aperture still remain open, as shown in Fig. 1, based on the results monitored in situ in the Yangzhuang Coalmine in Shandong Province, China (Wang et al. 2013). Thus, investigations of the mechanisms of cover stress re-establishment on the decrease in permeability of the WFFZ are needed for predicting and controlling the water inrush. The objectives of this paper are to investigate the processes and controlling factors affecting the decrease in fracture permeability due to the decrease in the fracture aperture and the mechanisms that control water inflow due to the cover stress re-establishment with a water inrush, using a case study from the Taiping Coalmine in Chinese Shandong Province.

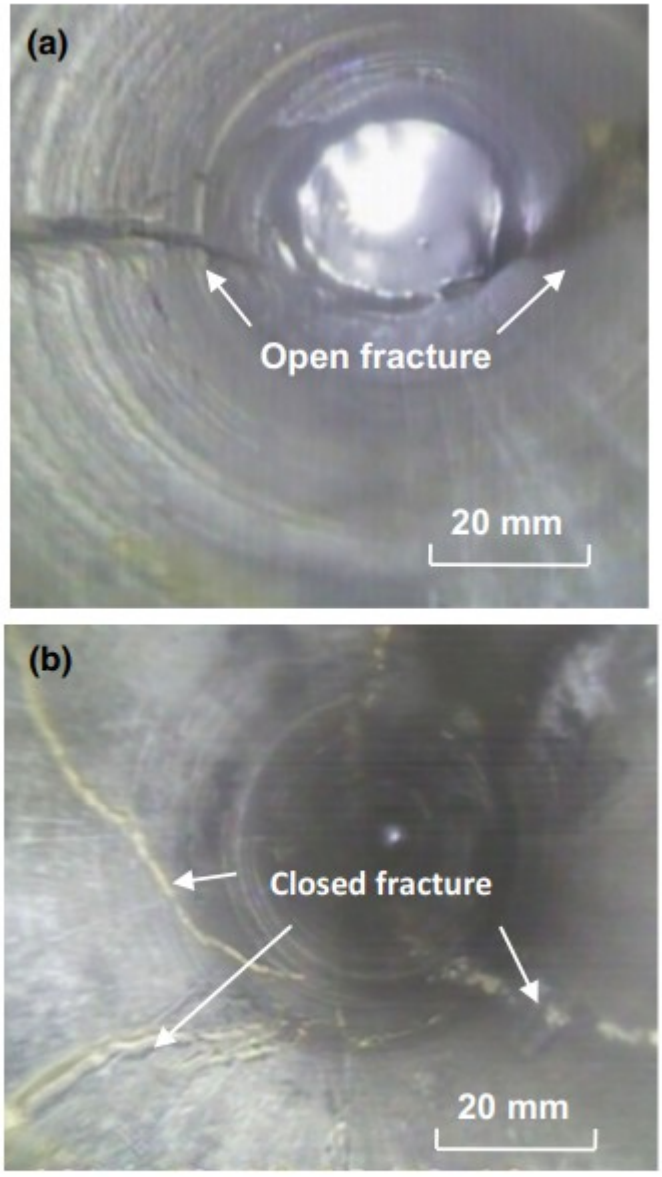

Fig. 1 The distribution of closed and open fractures in a monitoring borehole (Wang et al. 2013). **a** Open fracture at the height of 10.0 mabove the coal seam (the diameter of the hole is 91 mm). **b** Closedfracture at the height of 13.5 m above the coal seam (the diameter ofthe hole is 91 mm)

In this paper, the authors developed a conceptual model of the effective porosity of fractured rock mass, which is based on the bulking factor diminishing as a logarithmic function from bottom to top of the fractured rock mass caused by mining. The relationship between permeability of porous and fractured media was applied to develop a simplified fractured rock model. The aperture and permeability characteristics associated with the process of cover stress re-establishment were also investigated. Using the calculated permeability in the process of cover stress re-establishment,

water inflow into the panel was estimated and compared with the results of field observations.

Engineering geological conditions and water inrush progress

The Taiping Coalmine

The Taiping Coalmine is located in the southwestern part of the Yanzhou Coalfield, Shangdong, China (Fig. 2), and geologically located in the margin of the Western Shandong Block of the North China Platform. It has an area of 22 km^2, with a total geological reserve of 33 million tons and a designed length of service of 52 years. Since the 1990s, the Taiping Coalmine has produced about 1 million tons of coal annually under loose aquifers with the support of detailed and careful mining research and trials.

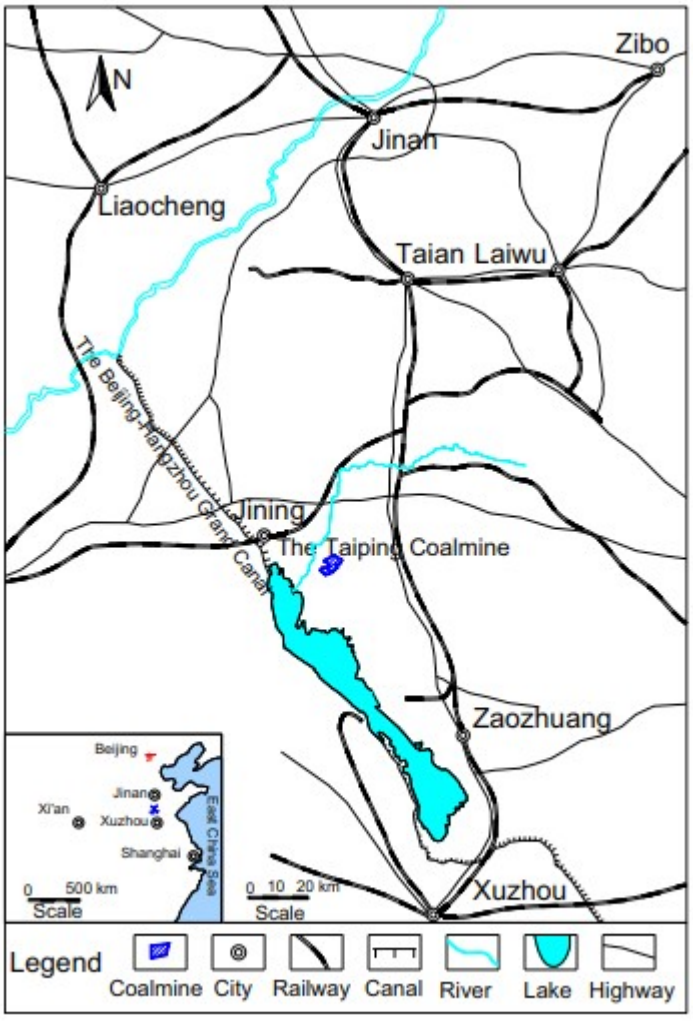

Fig. 2 Location of the Taiping Coalmine

The thickness of the primary coal seam, No. 3, is approximately 8.85 m on average with the overburden bedrock consisting of clayey sandstone, siltstone and fine and medium sandstones. The altitude of the coal measure

stratum is gentle with a dip angle of 5° to 15°. The strike directions of normal faults are usually in a north-to-south direction, while those of reverse faults are usually in an east-to-west direction.

The water inrush occurred in Panel S03, which belongs to southern part of the 6th district in the Taiping Coalmine (Fig. 3). This area is located in the rising end of syncline, as the coal measure stratum with a dip angle of 8° on average, much area of the coal seam is directly covered by the Quaternary unconsolidated formations with an average thickness of about 160 m. According to the borehole exploration results, the overburden bedrock thickness is from 0 to 32.6 m. Four panels are designed in the area with bedrock thickness more than 20 m based on the exploration results, Panel S01 to Panel S04 are excavated one by one. Accounting for a thin overburden rock and the unconsolidated aquifer, a method of slice mining is selected for Panel S03. The coal seam is designed to be excavated in four slices, each with a thickness of 2.2 m.

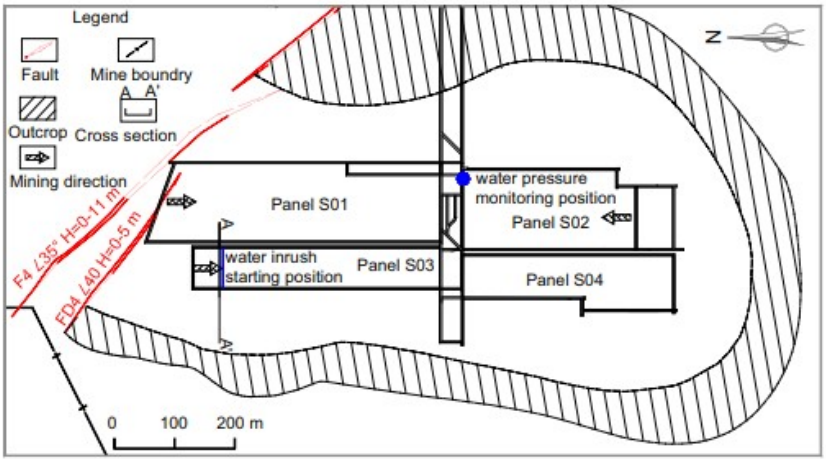

Fig. 3 The distribution of the panels in southern part of the 6th district

Overburden hydrogeology

The primary coal seam, No. 3, is affiliated to the Permian System, and the coal measures were directly covered by the Quaternary formations. The overburden can be divided into three aquifers and two aquifuges, based on its geological and hydrogeological characteristics. Two aquifers (Aquifers I and II) separated by Aquifuge I were distributed in the Quaternary formations. Aquifuge II is the weathered bedrock zone, separating Aquifer II hydraulic connection with Aquifer III compared with the clay seam at the bottom the Quaternary formations. The detailed properties of the aquifers and the aquifuges from top to bottom in the overburden are presented in the Table 1.

Table 1 Overburden hydrogeology in the Taiping Coalmine

System	Hydrogeological type		Thickness (m) $\frac{\text{Min}-\text{Max}}{\text{Ave.}}$	Hydrogeology
Quaternary (Q)	Upper group	Aquifer I	$\frac{54.25-71.5}{64.06}$	Strong confined porosity aquifers; composed by clay, sandy clay interbedded with clayey sand and sand; a specific capacity $q = 1.411–2.022$ L/sm; the mean water level is at EL. +47.64 to +48.58 m
	Middle group	Aquifuge I	$\frac{53.0-70.0}{61.5}$	Aquifuge, $q = 0.0436–0.2031$ L/sm; mainly composed by clay and clayed sand; the mean water level is at EL. +40.84 to +42.29 m; separating the hydraulic connection between the aquifer I and II
	Lower group	Aquifer II	$\frac{25.5-36.1}{30}$	Medium confined porosity aquifer, $q = 0.023–0.11$ L/sm; mainly composed by clay, clayed sand, medium and coarse sand interbedded; the mean water level is at EL. −45.69 to −46.0 m, the water pressure is 0.6 MPa; a coefficient of permeability $K = 0.183–1.47$ m/day, nonuniformity, the average value is about 1.0 m/day
		Clay seam	$\frac{0-10.9}{>2.0}$	Composed by clay and sandy clay; distribution at the bottom of the Quaternary formations, nonuniformity, some area disappears
Permian (P)	Bedrock weathering zone	Aquifuge II	$\frac{7.49-14.5}{10.95}$	Aquifuge of weathered mudstone and siltstone, abundant in weathered fractures, $q = 0.000729–0.000135$ L/sm
	Sandstone of roof	Aquifer III	$\frac{6.3-23.6}{13.0}$	Weak confined siltstone, fine and medium sandstone porosity and fissured aquifers, $q = 0.00069–0.00313$ L/sm

The sandstone (Aquifer III) is directly deposited on coal seam No. 3, which is the direct water filling aquifer for Panel S03 in the mining process. Aquifer II is the indirect water filling aquifer, unless the mining-induced fractures reach it. Most of the water in Aquifer III (sandstone) had been discharged or pumped out before coal mining. The normal water inflow of Panel S03 in the mining process is 15–20 m^3/h which is from Aquifer III in the fractured zone. According to the exploration results, the overburden bedrock above the coal seam No. 3 in Panel S03 is more than 22.8 m, and the in situ monitoring maximum WFFZ is 20.8 m with the coal mining thickness of 2.2 m. Compared with the clay seam with an average thickness of more than 2.0 m deposited at the bottom of Quaternary unconsolidated formations, in normal condition, the mining fractured zone does not reach Aquifer II.

Engineering geological conditions

The WFFZ only develops in the overburden bedrock in the mining process, thus the permeability evolution of the WFFZ is the most important factor in calculation of the water inflow change. The overburden bedrock is mainly composed of medium, silt and fine sandstone and mudstone. The surface of the bedrock had suffered different degrees of weathering, abundant in weathered fractures filling with argillaceous materials. The type of sandstone is mainly composed of quartz and feldspar. Due to the weathering and the inclination of coal measures, some strata disappear in the rising end. The strength of rocks adjacent to the Quaternary unconsolidated layers decreases significantly because of strong weathering. This kind of overburden structure is helpful for resisting the development of water flow fractured zone due to mining. The engineering geological types and the mechanical properties of the coal measures are presented in Table 2.

Table 2 Engineering geological types and mechanical properties of the coal measures

Engineering geological type	H (m)	σ_c (MPa)	τ (MPa)	E ($\times 10^3$MPa)	λ	c (MPa)	ϕ (°)
Mudstone	2.4	2.23	0.33	0.285	0.351	1.65	38
Silt–fine sandstone	16.0	30.60	1.60	1.87	0.23	6.25	36
Medium sandstone	4.0	22.40	1.46	2.15	0.208	1.57	37.8
Silt–fine sandstone	8.0	16.00	0.65	0.91	0.303	7.08	37
Fine sandstone	4.0	10.80	0.54	1.15	0.288	6.34	38
Coal seam No. 3	8.8	8.45	0.51	1.31	0.293	8.15	36
Fine sandstone	>10.0	29.90	1.49	4.01	0.261	15.1	33.5

H thickness, σ_c uniaxial compressive strength, τ tensile strength, E Young's modulus, λ Poisson's ratio, c cohesion, ϕ angle of internal friction

Water inrush process

According to the above analysis, the maximum height of WFFZ in Panel S03 is 20.8 m, which is less than the thinnest bedrock of 22.8 m above the coal seam No. 3. The water inrush from Aquifer II should not happen in the mining process. However, when the first slice of coal seam was excavated to a distance of 45 m, the water inflow in Panel S03 began to increase, and when excavation advanced to a distance of 50 m, the water inflow increased from 18 to 100–110 m^3/h. The maximum water inflow of 100–110 m^3/h continued for about 48 h with an advanced mining distance of about 4 m. At this stage, the aquifer water pressure at a distance of 400 m from the water inflow position decreased from 0.597 to 0.555 MPa. The water inrush and water pressure monitoring positions can be seen in Fig. 3. In the process of water inrush, the water inflow flowed down from different positions of the roof above the coal mining machine near the mining face and the collapsed gob, which was clean except for a small amount of turbidly at the beginning. When the advanced mining distance was 98 m, the water inflow diminished to 40–45 m^3/h. This stage lasted about 550 h and then the water inflow rate decreased slowly or kept relatively stable with advancing mining. At the same time, the aquifer water pressure increased to 0.597 MPa at the monitoring position. The water inflow process and the water pressure variations with the mining time and distance are shown in Fig. 4, which indicated that the WFFZ has penetrated into Aquifer II. The chemical characteristics of drainage also confirmed the groundwater was from Aquifer II. Accounting for the bedrock's geological sedimentary inhomogeneity and the boreholes exploration results around the water inrush position, the thickness of the bedrock may be less than 20.8 m and the clay seam does not exist at the water inrush position. A simplified cross section along profile line AA' (Fig. 2) is shown in Fig. 5. In this figure, the cross section ranges from EL. −40.0 to EL. −160.0 m in a vertical direction, not including the ground surface with an elevation of +42.0 m on average. The water inrush schematic diagram also is shown in Fig. 5, which will be introduced in the "Prediction of water inflow resulting from the cover stress re-establishment".

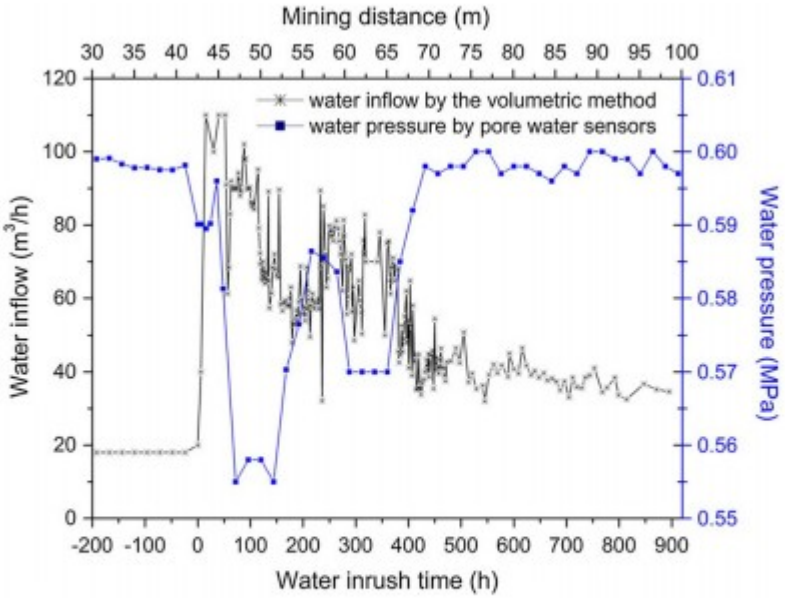

Fig. 4 In situ monitoring of water inflow and pressure variations within water inrush time and mining distance

Fig. 5 Schematic diagram of the water flowing into Panel 03 from a confined aquifer due to coal mining

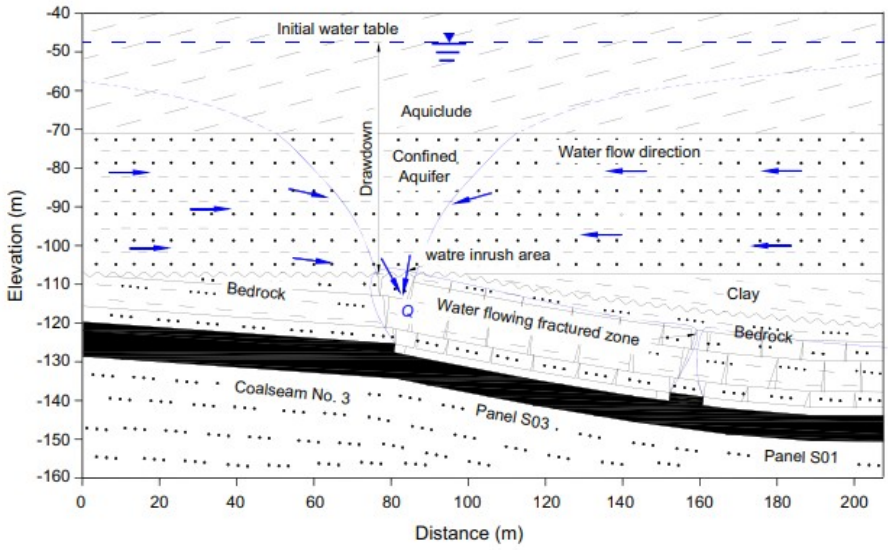

The fact that the subsidence of upper strata and the vertical cover stress re-establishment resulted in decreasing the permeability of the induced fractures is the main reason why the water inflow decreased as the excavation of coal seam continued.

Fracture model of WFFZ

Basic assumptions for calculations

Two models are used in the calculations: (a) a porous media model, and (b) a fractured-porous media model. The porous model can be used to describe

the permeability variation of the overburden zone after coal mining activities. The fractured-porous media model can be used to calculate the permeability change and deformation of the fractured rock mass during the cover stress re-establishment. The basic assumptions for the two models are as follows:

1. Water flow is two-dimensional and can be described by Darcy's law.

2. The increase of water inflow during water inrush is caused by coal mining-induced fractures.

3. The cover stress re-establishment causes the rock fracture permeability to decrease, but its effect on the rock matrix has been mostly ignored, the same on the deformation.

4. The porosity and permeability in the caving zone are uniform, and the effect of heterogeneity is not considered.

5. The water pressure on the fracture surface, during the water inrush, is zero.

Permeability distribution of the WFFZ

Based on the in situ monitoring data, Guo et al. (2002) determined that the lumpiness of fractured rock increased quickly as the distance from the level of the gob increased, and the remnant bulking factor reduced gradually as a logarithmic function. Assuming a uniform distribution of the bulking factor in the caving zone, Shao et al. (2011) proposed a relationship to describe a permeability distribution in the fractured zone, but without taking into consideration the displacement Δh. In consideration of the displacement Δh (see Fig. 6), the bulking factor distribution b_z at the elevation z above the gob in fractured rock mass due to coal mining can be given by:

$$\begin{cases} b_z = b, & 0 \le z \le h_c - \Delta h \\ b_z = b - c_k \cdot \ln(z + 1 - h_c + \Delta h), & h_c - \Delta h \le z \le h_c + h_f \end{cases} \quad (1)$$

where

$$b = b' - \frac{\Delta h}{h_c} \quad (2)$$

$$c_k = (b - b_z^B)/\ln(h_f + \Delta h + 1) \quad (3)$$

b_z is the bulking factor at the elevation z above the gob, b' is the bulking factor in the gob prior to the formation of the fractured zone, b is the bulking factor in the gob after the formation of the fractured zone, c_k is the attenuation ratio of the gob bulking factor in the vertical direction, and $b_z^B = 1$ is the bulking factor at the juncture of the caved and bending zones,

h_f is the height of fractured zone, h_c is the height of caving zone, m is the thickness of mining coal, Δh is the compressive displacement in the process of the fractured zone forming.

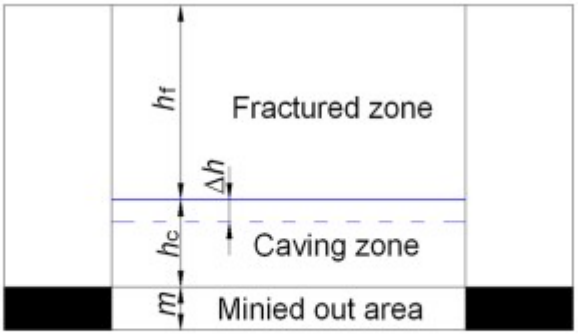

Fig. 6 Formation relationship between the caving zone and fractured zone

Prior to the surface subsidence, the volume of excavated coal seam is equal to the total void volume in the caving zone and fractured zone, and is given by:

$$m = h_c \cdot (b - 1) + \int_{h_c - \Delta h}^{h_c + h_f} (b_z - 1)\mathrm{d}z. \tag{4}$$

Based on a simplified porous medium model, the effective porosity of the fractured rock mass can be given by:

$$n_z = 1 - 1/b_z \tag{5}$$

where n_z and b_z are an effective porosity and a bulking factor, respectively, both of which change over the height of the fractured rock mass. The permeability of porous medium can be calculated with the Blake–Kozeny formula given by:

$$\begin{cases} k_0 = \dfrac{\phi^2}{150}\left(\dfrac{n_0^3}{(1-n_0)^2}\right) \\ k = \dfrac{k_0}{0.241}\left(\dfrac{n^3}{(1-n)^2}\right) \end{cases} \tag{6}$$

where k_0 is the initial permeability of the caving zone, ϕ is the diameter of the rock fragments, n_0 is the initial porosity, n is the porosity, and k is the permeability.

By substituting Eqs. (1) and (5) in Eq. (6), the relationship between permeability and the bulking factor of the fractured rock mass can be expressed as:

$$\begin{cases} k = k_0, & 0 \le z \le h_c - \Delta h \\ k = \frac{k_0}{0.241}\left(\frac{(b' - c_k \cdot \ln(z + 1 - h_c + \Delta h) - 1)^3}{b' - c_k \cdot \ln(z + 1 - h_c + \Delta h)}\right), & h_c - \Delta h \le z \le h_c + h_f \end{cases} . \quad (7)$$

The hydraulic conductivity of the porous medium can be expressed as:

$$K = \frac{k \cdot \gamma}{\mu} \quad (8)$$

where K is the hydraulic conductivity, k is permeability, γ is the unit weight of liquid, and μ is the liquid kinematic viscosity.

Fracture aperture distribution in WFFZ

The fractured medium can be represented using a simplified porous medium model (Liu et al. 1999), if the angle between two fractures is $\theta = \frac{360^\circ}{2n}$. In this study, the simplified two-dimensional plane porous medium model is used assuming that water flow through a unit width of porous media is equivalent to the flow in a fracture. In this paper, the subscript 'p' and 'f' indicate porous medium and fractured medium, respectively:

$$Q_p = Q_f \quad (9)$$

where Q_p is the water inflow of a porous medium, Q_f is the water inflow of a fractured medium, and the expression for the hydraulic conductivity K_p of the equivalent porous medium is given by:

$$K_p = \frac{K_f \cdot d \cdot \sin\alpha}{s} \quad (10)$$

where K_f is the hydraulic conductivity of the fractured medium, s is the unit width of porous medium and also the spacing between two fractures in fractured medium, d is the aperture of the fracture, and α is the angle of the fracture with horizontal plane. A fracture hydraulic conductivity can be given by:

$$K_f = \frac{\rho g d^2}{12\mu}. \quad (11)$$

By substituting Eq. (10) in (9), the fracture aperture can be given by:

$$d = \left(\frac{12\mu s K_p}{\rho g \cdot \sin\alpha}\right)^{\frac{1}{3}}. \quad (12)$$

By substituting Eq. (7) in (12) subject to the condition of $h_c - \Delta h \le z \le h_c + h_f$, the fracture aperture can be expressed using the bulking factor:

$$d = \left(\frac{12\,\mu s}{\rho g \sin\alpha} \cdot \frac{k_0}{0.241} \cdot \frac{(b' - c_k \cdot \ln(z + 1 - h_c + \Delta h) - 1)^3}{b' - c_k \cdot \ln(z + 1 - h_c + \Delta h)} \right)^{\frac{1}{3}}. \quad (13)$$

Field observations in Panel 03 of the Taiping Coalmine showed that the height of WFFZ in the fractured zone is 20.8 m, and the caving zone height is 7.3 m, using Eqs. (1–4), Δh = 0.81 m and an initial b = 1.19 are gained. The average diameter of rock fragments in the caving zone was chosen as 0.5 m, and $\gamma = 1 \times 10^4$ N/m^3, $\mu = 1 \times 10^3$ N s/m, using Eqs. (7) and (8), the hydraulic conductivity distribution in the WFFZ (Fig. 7) shows that the hydraulic conductivity decreases dramatically from the bottom to the top of the fractured zone, from 2.39 to 6.5 × 10^{-9} m/s.

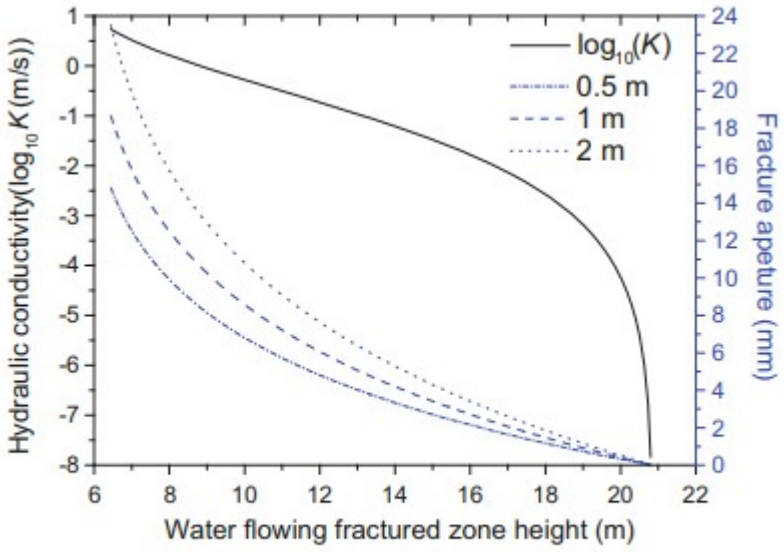

Fig. 7 Hydraulic conductivity distribution in fractured zone

According to the hydraulic conductivity distribution in the fractured zone, assuming the angle between the fracture and a horizontal plane is 90°, for the fracture spacing of 0.5, 1.0 and 1.5 m, respectively, using Eq. (13), the fracture apertures distribution in the WFFZ are also shown in Fig. 7. This figure shows that the fracture apertures increase as the fracture spacing increases, and decrease from the bottom to the top of the fractures.

Permeability evolution of the WFFZ with the cover stress re-establishment

Stress–strain characteristics

Fractured or porous rock differs from purely solid materials in that it is inherently heterogeneous, and includes both a solid phase and fractures (and/or pores) with a variety of geometric shapes (Liu et al. 2009). While the elastic strain is indeed small in most of the rock for stress changes of practical interest, the strain can be considerably larger within some portions of a rock body. For example, some fractures (or large pores) in a rock can be

subject to significant deformation, and even completely closed under a certain range of stress changes encountered in practice. For these fractures, the strain is not small (i.e., on the order of one). To simplify the equations describing permeability, it is reasonable to assume that the fractured rock mass can be represented as poroelastic continuous media (Oda 1986; Zhu and Wang 1993; Pariseau 1993). This section focuses on the fracture aperture deformation and permeability evolution under normal stress, using a conceptual model shown in Fig. 8. The relationship between σ_1 and σ_3 can be expressed as:

$$\sigma_3 = \lambda \sigma_1 \tag{14}$$

$$\lambda = \frac{\mu}{1-\mu} \tag{15}$$

where λ is the lateral pressure coefficient, and μ is Poisson's ratio.

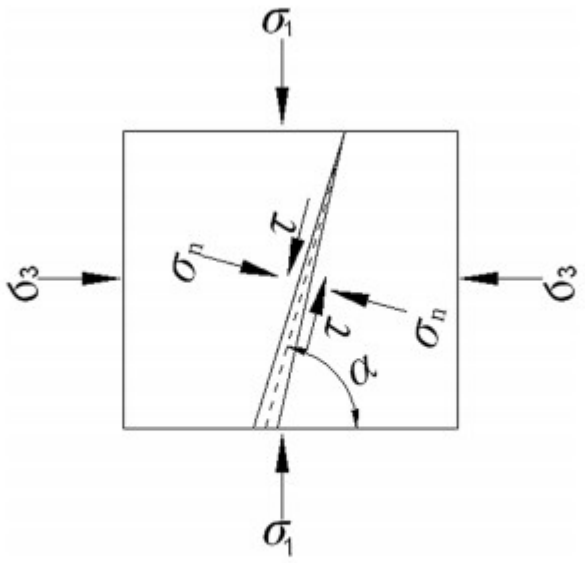

Fig. 8 Conceptual model for the effect of a fracture subjected to stress; where σ_1 is the vertical stress, σ_3 is horizontal stress, σ_n is normal stress on the fracture, τ is the shear stress on the fracture, and α is the angle between the fracture and horizontal line

To evaluate the stress–strain characteristics of a fracture, the angle α is assumed as 90° because the vertical permeability is focused in this study. The deformation of the fractured rock mass includes the deformations of the rock matrix and fracture:

$$u_{\mathrm{t}} = u_{\mathrm{m}} + d_{\mathrm{n}} \tag{16}$$

$$s\varepsilon_{\mathrm{t}} = (s-d)\varepsilon_{\mathrm{m}} + d\varepsilon_{\mathrm{d}} \tag{17}$$

where u_t and ε_t are the rock mass deformation and strain, u_m and ε_m are the rock matrix deformation and strain, d_n and ε_d are the fracture deformation and strain, respectively, s is the spacing between two fractures, and d is the aperture of the fracture.

Based on laboratory experiments on rock fractures in dolerite, limestone, siltstone and sandstone, Bandis et al. (1983) proposed a hyperbolic function to express the normal effective stress–closure relation of a fracture. Assuming positive signs for compression and fracture closure and negative signs for tension and fracture opening, the normal effective stress–closure relation is given by:

$$d_n = \frac{\sigma_n}{k_n + (\sigma_n / d_{max})} \tag{18}$$

where σ_n is the normal effective stress, d_n is the fracture closure, d_{max} is the maximum allowable closure, and k_n is the normal stiffness of the fracture at initial stress. When the normal stress becomes infinite, fracture closure approaches the maximum allowable fracture closure, and simultaneously, normal fracture-specific stiffness becomes infinite. By substituting Eq. (18) in (17),

$$\frac{s\sigma_n}{E_{mass}} = \frac{(s-d)\sigma_n}{E_{matrix}} + \frac{\sigma_n}{k_n + (\sigma_n / d_{max})}. \tag{19}$$

Here

$$\begin{cases} \sigma_n = \sigma_3 \sin^2\alpha + \sigma_1 \cos^2\alpha \\ \tau = \frac{1}{2}(\sigma_1 - \sigma_3)\sin 2\alpha \end{cases} \tag{20}$$

where E_{mass} is the rock mass bulk modulus, E_{matrix} is the rock matrix bulk modulus, and k_n is the normal stiffness of the fracture.Accounting for a fracture angle, by substituting Eq. (20) in (19), Eq. (19) can be expressed as:

$$\frac{\mu s\sigma_1}{E_{mass}} = \frac{(s-d)\cdot[\mu\sigma_1 \sin^2\alpha + (1-\mu)\sigma_1 \cos^2\alpha]}{E_{matrix}} + \frac{\mu\sigma_1 \sin^2\alpha + (1-\mu)\sigma_1 \cos^2\alpha}{k_{ni} + [\frac{\mu}{(1-\mu)}\sigma_1 \sin^2\alpha + \sigma_1 \cos^2\alpha]/d_{max}}. \tag{21}$$

The rock matrix deformation is much smaller compared with the fracture deformation under the same stress. If the deformation of the matrix in calculating the aperture deformation is ignored, the aperture deformation can be expressed as:

$$\Delta d = \frac{\sigma_1(\frac{\mu}{1-\mu}\sin^2\alpha + \cos^2\alpha)}{k_{\mathrm{ni}} + [\sigma_1(\frac{\mu}{1-\mu}\sin^2\alpha + \cos^2\alpha)/d_{\max}]}. \quad (22)$$

When the aperture has a deformation of Δd, based on Eq. (11), the permeability can be expressed as:

$$K'_{\mathrm{f}} = \frac{\rho g(d - \Delta d)^2}{12\,\mu}. \quad (23)$$

Assuming the fracture angle of 90, and using Eq. (10), the expression for hydraulic conductivity K'_f of a fracture under normal stress can be written as:

$$K'_p = \frac{K'_f(d - \Delta d)}{s - \Delta d} = \frac{\rho g(d - \Delta d)^3}{12\mu(s - \Delta d)} \quad (24)$$

where K'_f is the hydraulic conductivity of a fracture under normal stress, Δd is the fracture closure under normal stress, K'_{p} is the equal hydraulic conductivity of porous medium under stress.

In Panel S 03 of the Taiping Coalmine, the tectonic structure is simple, the strata mainly bear the gravity stress, so the σ_1 in Eq. (22) is equivalent to the vertical stress σ_v, which has decreased due to coal mining and will generally re-establish as the mining distance increased.

Characteristics of cover stress re-establishment in WFFZ

Measurement of deformations and stresses in the gob are difficult due to the inaccessibility of the waste area. Most of researchers used a linear function to estimate the cover stress re-establishment distance (King and Whittaker 1971; Choi and McCain 1980; Mark 1992). Yavuz (2004) used a non-linear empirical formula to estimate the cover stress re-establishment distance in the gob based on surface subsidence, which is adopted in this paper.

According to the profiles drawn by British National Coal Board for predicting the maximum subsidence in relation to the width of the panel, depth and height of the excavation by evaluating the measurements from British coalfields over some years, Yavuz (2004) derived two empirical formulae to estimate the cover stress re-establishment distance X_a and the stress at a distance X in the gob with the surface subsidence value when the gob stress recovered:

$$X_a = 0.2H^{0.9}6^{S_m/m}, \quad R^2 = 0.993 \tag{25}$$

$$\sigma_X = \sigma_V \left[1.02 - 1.76\left[\frac{S_m}{m}\right] - 0.14\left[\frac{X}{X_a}\right] + 0.44\left[\frac{S_m}{m}\right]^2 + 0.6\left[\frac{X}{X_a}\right]^2 + \left[\frac{S_m}{m}\right]\left[\frac{X}{X_a}\right] \right], \quad R^2 = 0.98 \tag{26}$$

where S_m is the subsidence depth on the surface when the cover stress re-establishment, how to calculate this value will be introduced in the following section.

Equation (26) is applicable for X/X_a ratios between 0.2 and 0.8, since the data points between these ratios were used for the regression analysis. For X/X_a ratios of 0 and 1, σ_x/σ_v ratios should be assigned as 0 and 1, respectively.

Pappas and Mark (1993) investigated how the gob would exhibit the strain hardening behavior, as the material becomes stiffer and the modulus increases under the condition of the load increases. With the increase in the size of fragments, the strain decreases under high-stress conditions at the later time. They also found that the stress–strain characteristics have little relation to the rock type.

Accounting for the characteristics of the caved rocks, Salamon (1990) suggested the following equation for the backfill material to describe the stress–strain behavior of gob material:

$$\sigma = \frac{E_0 \varepsilon}{1 - \varepsilon/\varepsilon_m} \tag{27}$$

where

$$\varepsilon_m = \frac{b-1}{b}. \tag{28}$$

By substituting Eq. (28) in (27), the strain, when subjected to stress, can be expressed by:

$$\varepsilon = \frac{(b-1)\sigma}{(b-1)E_0 + b\sigma} \tag{29}$$

where ε is the strain occurring under the applied stress, E_0 is the initial tangent modulus, σ is the applied stress, and ε_m is the maximum possible strain of bulked rock material.

When the material in the gob is subjected to the recovery stress, the bulking factor will diminish as the volume of the material decrease in the gob.

Therefore, the stress–strain relationship of material in the gob can be expressed by:

$$\varepsilon = \frac{(b - b_s)h_c}{m + h_c} \tag{30}$$

where b_s is the bulking factor of the caving zone under recovery stress. By equating Eqs. (29) and (30), the bulking factor of the caving zone under recovery stress can be given by:

$$\frac{(b - b_s)h_c}{m + h_c} = \frac{(b - 1)\sigma}{(b - 1)E_0 + b\sigma} \tag{31}$$

$$b_s = b - \frac{(b - 1)\sigma}{(b - 1)E_0 + b\sigma} \cdot \frac{m + h_c}{h_c}. \tag{32}$$

Yavuz (2004) proposed the following formula for E_0:

$$E_0 = \frac{10.39\sigma_c^{1.042}}{b^{7.7}} \tag{33}$$

where σ_c is the uniaxial compressive strength of rock.

By substituting Eq. (32) and $\sigma = \gamma H$ in Eq. (33), the bulking factor of the gob under recovery stress can be given by:

$$b_s = b - \frac{(b - 1)\gamma H}{\frac{(b-1)10.39\sigma_c^{1.042}}{b^{7.7}} + b\gamma H} \cdot \frac{m + h_c}{h_c}. \tag{34}$$

The excavated volume of coal can be calculated using the void volumes in the caving zone and fractured zone, as well as the subsidence volume at the surface:

$$S_m = m - h_c \cdot (b_s - 1) - \int_{h_c - \Delta h}^{h_c + h_f} (b_z - 1)dz. \tag{35}$$

By substituting parameters given in Table 3 in Eqs. (34) and (35), the surface subsidence was calculated to be 0.93 m. Then, the stress recovery distance was calculated to be 46.8 m, using Eqs. (25) and (26).

Table 3 Parameters used for calculation using empirical formulas [Eqs. (26), (27)]

H (m)		m (m)	γ (kN/m^3)		σ_c (MPa)	μ	b	h_c (m)	h_f (m)
Soil	Rock		Soil	Rock					
160	25	2.2	20	22	13.2	0.35	1.19	7.3	13.5

The unit weight and thickness of the strata, uniaxial compressive strength and Poisson ratio in this table are the average values, σ_c is the average compressive strength of rock mass in caving zone

Figure 9 depicts the calculated vertical stress distribution above the fractures in the process of cover stress re-establishment. Because Eq. (26) is

applicable for X/X_a ratios between 0.2 and 0.8, as X/X_a ratios of 0 and 1, σ_X/σ_V ratios should be assigned as 0 and 1, respectively.

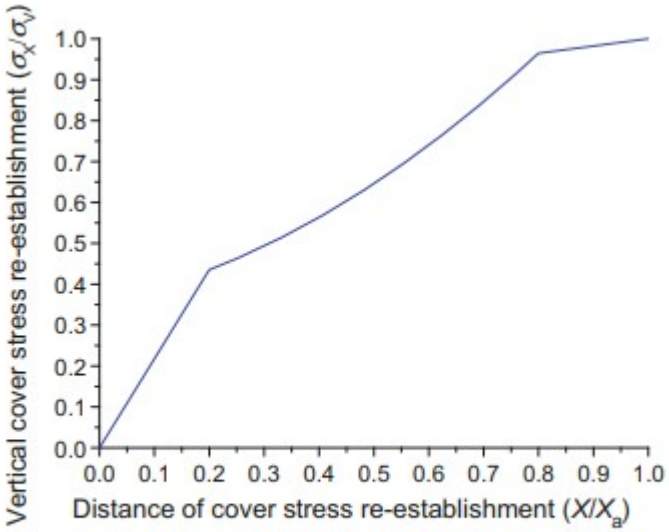

Fig. 9 Calculated vertical cover stress re-establishment distribution above the fractures

The horizontal stress also increases with depth which can be calculated with the lateral pressure coefficient of the rock mass based on the vertical stress.

Changes in the apertures and hydraulic conductivities due to stress re-establishment

The mechanism of fracture deformation and the function describing the cover stress re-establishment have been discussed in “Stress-strain characteristics” and “Characteristics of cover stress re-establishment in WFFZ”. However, the stiffness of the fracture in the fractured zone due to coal mining is still an unknown parameter. Generally, the initial contact area, aperture distribution, small-scale roughness, strength and deformability of asperities, and thickness, type and physical properties of infilling material will affect the normal stiffness of a rock fracture (Steer et al. 2011; Worthington and Lubbe 2007; Baghbanan and Jing 2008). For different monitoring methods, the normal stiffness of a rock fracture may vary several orders of magnitude. In the following calculations, the overburden rock has an average uniaxial compressive strength less than 20 MPa, the fractures without infilling in the overburden rock are generated due to coal mining, and very small or no stress is initially applied on the fractures. Based on in situ monitoring results (Steer et al. 2011; Worthington and Lubbe 2007; Baghbanan and Jing 2008; Hardin et al. 1987; Lubbe and Worthington 2006; Fransson et al. 2010; Lee and Harrison 2001), the smallest stiffness of 0.1 GPa/m is selected at the fracture bottom in the fractured zone. In consideration of the aperture’s influence on the stiffness of the fracture, the

stiffness increases linearly with a coefficient of 0.23 along the fracture to the top of the fractured zone.

According to the results of field measurements, the fracture spacing and the fracture angle are selected as 0.5 m and 90°. Application of the rule of cover stress re-establishment in the Eqs. (22) and (24), the decrease of the fracture aperture and the hydraulic conductivity evolution in the fractured zone during the cover stress re-establishment are shown in Figs. 10 and 11, respectively.

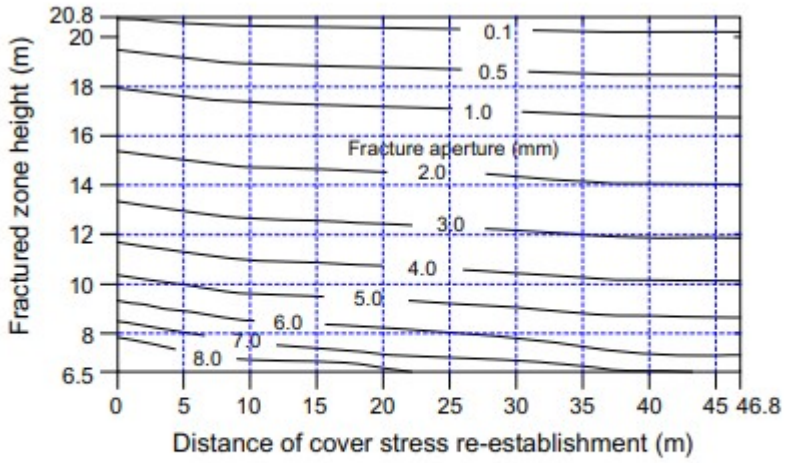

Fig. 10 Fracture aperture change with cover stress re-establishment distance

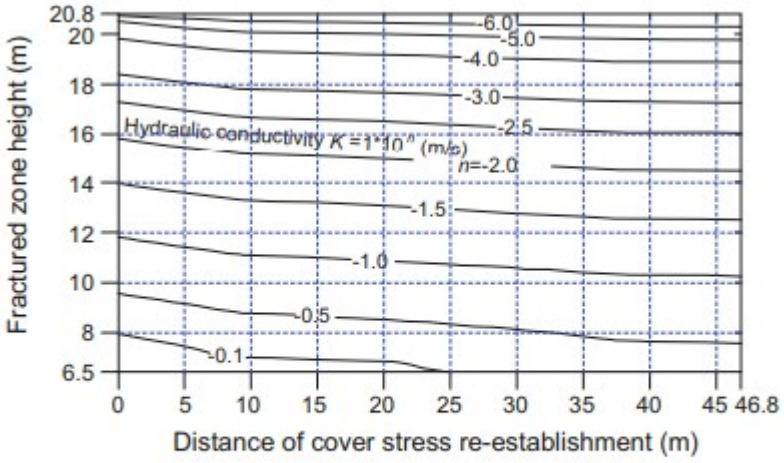

Fig. 11 Hydraulic conductivity change with cover stress re-establishment in fractured zone

These figures indicate that the aperture and permeability at the lower parts of the fractured zone are greater than the upper parts, and both of them decrease with the cover stress re-establishment. The aperture and

permeability in the lower parts decrease more significantly, but are still greater than the upper parts when the cover stress has completely re-established. The permeability in the weathered fractured rock near the top of the fractured zone decreases to a very low level and the water-resisting property generally recovers with the cover stress re-establishment.

Prediction of water inflow resulting from the cover stress re-establishment

When the fractures develop and propagate into the aquifer due to coal mining, the water inflow increases in the mining panel, as shown in Fig. 5. The value of the water inflow depends on the flow area, water pressure, aquifer thickness, and the hydraulic conductivity of rock within the water inrush area. As an analog to the water inrush into the coal mine, the radial groundwater flow through a confined, horizontal, uniformly thick, homogeneous, and isotropic aquifer, with an infinite areal extent, was assumed, as described by the Theis equation (Theis 1935) given by:

$$s(r,t) = \frac{Q}{4\pi T}\int_u^\infty \frac{e^{-u}}{u}\mathrm{d}u \tag{36}$$

where

$$u = \frac{r^2\mu^*}{4Tt} \tag{37}$$

where s is drawdown, Q is discharge (assuming a constant pumping rate), T is transmissivity, t is time since pumping began, r is radial distance from the pumping well, and μ^* is storativity.

From Eq. (36), the hydraulic gradient $I(r,t)$ at a distance r from the pumping well can be calculated as:

$$I(r,t) = -\frac{Q}{2\pi T r}\exp\left(-\frac{r^2\mu^*}{4Tt}\right). \tag{38}$$

For large t and large r, the water flow is nearly in steady state, for $t \geq 25\frac{r^2\mu^*}{T}$, $\exp(-\frac{r^2\mu^*}{4Tt}) = 0.99 \approx 1$, then, $Q_r = Q$, where Q_r is the rate of water flow through the aquifer section at a distance of r from the pumping well. At the distance of r from the pumping well, the hydraulic gradient can be given by:

$$I = \frac{Q}{2\pi T r}. \tag{39}$$

During the water inrush into the coal mine, the water head above the water inrush area declines to zero rapidly (Zhang et al. 2006), so that the confined aquifer transforms into an unconfined aquifer around the water inrush area.

The water inflow can be calculated using the equation for a confined–unconfined aquifer given by:

$$Q = \frac{1.366K(2h_0M - M^2)}{\lg R - \lg r_w} \quad (40)$$

where h_0 is the water head of the aquifer before pumping, R is the radius of influence, M is the thickness of the aquifer, and r_w is the radius of water inrush area. By substituting Eq. (40) in Eq. (39), the hydraulic gradient above the water inrush area can be expressed by:

$$I = \frac{1.366(2h_0 - M)}{2\pi r(\lg R - \lg r_w)}. \quad (41)$$

When $r = r_w$, Eq. (41) can be rewritten as:

$$I = \frac{1.366(2h_0 - M)}{2\pi r_w(\lg R - \lg r_w)}. \quad (42)$$

At a certain distance from the water inrush area, the water head decreases below the roof of the confined aquifer. Outside of this area the water head is still above the roof of the aquifer, and the rate of water flow can be given by:

$$Q = -2\pi rM(-K\frac{dh}{dr}) = 2\pi rT\frac{dh}{dr}. \quad (43)$$

This equation can be integrated to obtain an expression for the groundwater head h

$$h = \frac{Q}{2\pi T}\ln r + c \quad (44)$$

where c is an integration constant, which can be obtained by stating that at a distance R (i.e., radius of influence) from the well the groundwater head is equal to its background level h_0. The drawdown s at a distance of r can be expressed by:

$$\Delta h = h_0 - h = \frac{Q}{2\pi T}\ln\left(\frac{R}{r}\right). \quad (45)$$

From Eq. (45), using the data shown in Fig. 4, the relationship between the rate of water inflow and the radius of influence was calculated as a linear regression ($R^2 = 0.925$), and the results are shown in Fig. 12.

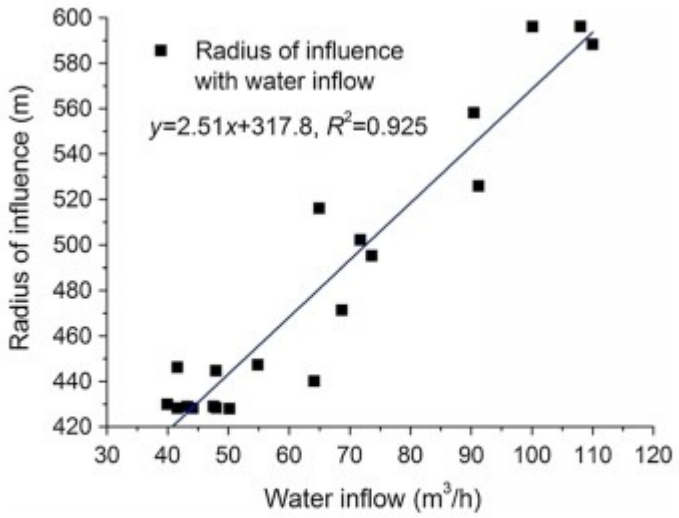

Fig. 12 The relationship between the water inflow and the radius of influence

By substituting the linear relationship in Fig. 12 in Eq. (42), the hydraulic gradients for different water inflow rates can be calculated from:

$$I = \frac{1.366(2h_0 - M)}{2\pi r_{\mathrm{w}}[\lg(2.51Q + 317.8) - \lg(r_{\mathrm{w}})]}. \tag{46}$$

As stated above, the cover stress re-establishment does not change the radius of the water inrush area, but causes the permeability of the rock mass within the water inrush area to decrease. Using Eq. (41), the radius of the water inrush can be calculated from the equation given by:

$$r_{\mathrm{w}} = 10^{(\lg(R) - \frac{1.366K(2h_0M - M^2)}{Q})}. \tag{47}$$

By substituting the maximum rate of the water inflow and other parameters which are listed in Table 4 in Eq. (47), the radius of the water inrush area is calculated to be 4.7 m. The water inflow though the water inrush area during the cover stress re-establishment can be given by:

$$Q = K_{\mathrm{p}} \cdot I \cdot F. \tag{48}$$

By substituting Eq. (46) in Eq. (48), the water flow in the process of cover stress re-establishment is given by:

$$Q = K_{\mathrm{p}} \cdot \frac{1.366(2h_0 - M)}{2\pi r_{\mathrm{w}}[\lg(2.51Q + 325.8) - \lg(r_{\mathrm{w}})]} \cdot F. \tag{49}$$

Table 4 Parameters of water inflow calculation

Q_{max} (m^3/h)	K (m/day)	h_0 (m)	M (m)	Δh (m)	r_m (m)
100 ~ 110	1.5	60.0	30.0	4.4–4.6	420

r_m is the distance from the water head monitoring site to water inrush area

The parameters given in Table 4 were also used to predict the water inflow from Eq. (49). Figure 13 demonstrates that the predicting water inflow using Eq. (49) with the hydraulic conductivities variation at the height of 19.0 in the process of cover stress re-establishment is in a good agreement with the in situ monitoring data. One can see from Fig. 13 that the in situ monitoring data of water inflow fluctuated more obviously than calculation results, as shown in Fig. 13, which may have been caused flow through a complex fracture network, with fractures' closure, new fractures formation generating besides them and materials flowing with water short-blocking the flow pathways. The hydraulic conductivities at the heights of 19.0 m vary from 2.28×10^{-4} to 2.67×10^{-5} m/s in the process of cover stress re-establishment. Outside of the stress re-establishment zone the water inflow still reduces slowly, which could be affected by other factors like rock softening and expansion with longtime encountering water or fracture infilling reducing the fracture aperture.

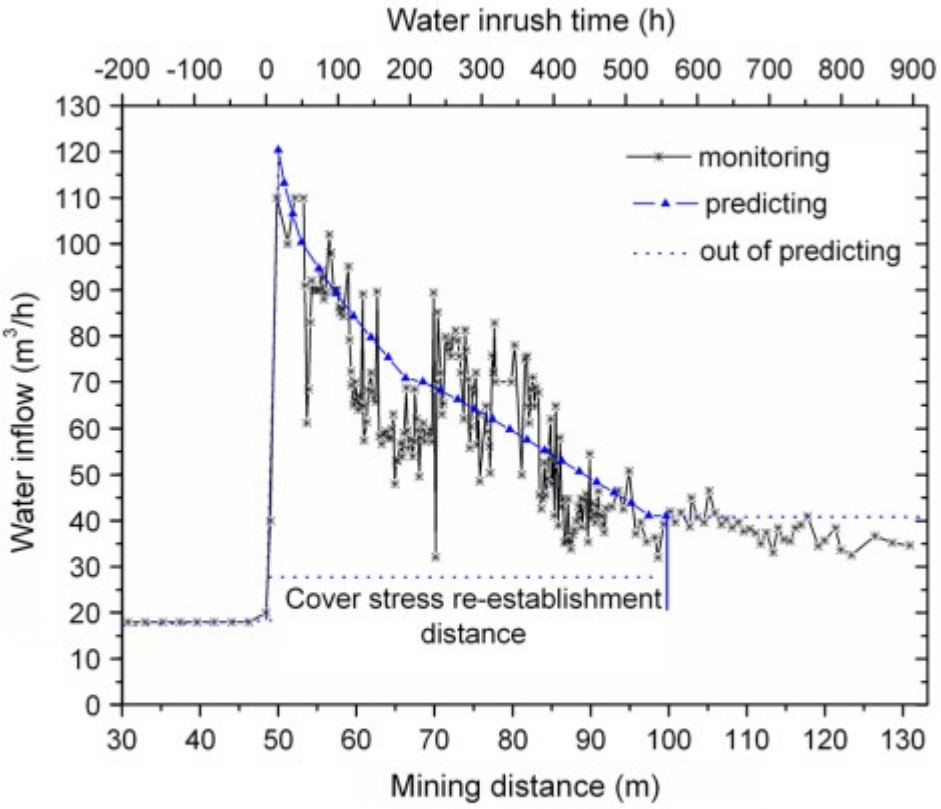

Fig. 13 Relationship between monitoring and predicting water inflow

Discussions and conclusions

It is generally known that the permeability in the upper parts of the fractured rock mass due to coal mining is greater than that in the lower ones. The permeability depends on the fractures evolution which induces the increase in the bulking factors. However, there is no general applicable formula to describe the permeability distribution in the mining-induced fractured rock mass. The results of calculations in this paper confirm the conclusions of Guo et al. (2002), who, based on the results of in situ monitoring, found that the remnant bulking factor reduced gradually as a logarithmic function as the distance from the level of the gob increased.

The in situ monitoring data and semi-analytical calculations of the groundwater inrush into a panel of the Taiping Coalmine of Shandong Province, China show that the permeability of mining-induced fractured rock mass decreases due to cover stress re-establishment after coal mining. The results of calculations, using a porous media model to describe the permeability distribution in the disturbed overburden rock mass after coal mining, show that the permeability in the fractured zone varies several orders of magnitudes from the bottom to the top.

The surface subsidence above Panel S03 in the Taiping Coalmine, when the cover stress had been totally re-established, was estimated to be 0.93 m. The cover stress re-establishment distance was calculated to be 46.8 m.

The permeability in the lower part was much greater than the above part in the water flow fractured zone, though the permeability decreased more during the cover stress re-establishment. Different hydraulic conductivities were applied to calculate the water inflow, a good agreement between the prediction and in situ monitoring inflow rate was achieved with using the hydraulic conductivity at the height of 19.0 m in the water flow fractured zone. In the calculation, the fracture dip angle was assumed to be 90°. The fractures in the water flow fractured zone with smaller dip angles generate greater closure and keep less residual hydraulic conductivity in the process of cover stress re-establishment. Thus, if different dip angles (smaller than 90°) of fractures are considered in the water flow fractured zone, a hydraulic conductivity at a little lower position than 19.0 m may generate the same evolution as that at the height of 19.0 m with the fracture dip angle of 90° in the process of cover stress re-establishment, which would be suitable for calculating water inflow.

At the water inrush sites on the contact surface of the bedrock and the Aquifer II, the water flows to the lower fractured rock mass only through the vertical fractures, which are like an entrance with the minimum opening determining water inflow. The two-dimensional model can be used to analyze the permeability evolution with cover stress re-establishment for calculating the water inflow, and reflects the vertical permeability evolution of the fractured rock mass with the same horizontal permeability in different directions at the same elevation.

Thus, the results of this study improved the understanding of the mechanisms of the post-mining cover stress recovery and the permeability change in the overburden fracture rock strata, which then can be applied to numerically simulate the process of overburden failure and consequent groundwater inrush due to coal mining. However, this two-dimensional model does not fully account for the anisotropic permeability, which can be simulated using a three-dimensional model of the fracture network. The authors recognize that more research is needed in the future on the permeability distribution in the fractured rock mass due to coal mining and on the reliability of the method proposed in this study.

Acknowledgments

Financial support of the National Natural Science Foundation of China under Grant No. 41172291, 973 Program under Grant No. 2013CB227903, a Project Funded by the Priority Academic Program Development of Jiangsu Higher Education Institutions, Henan institution of higher education key scientific research project (16A 410004), and a high-level personnel scientific research startup project of North China University of Water Resources and Electric

Power (40470) is acknowledged. The authors also sincerely thank Gregory Weissmann at University of the Pacific for his editorial help.

References

Baghbanan A, Jing L (2008) Stress effects on permeability in a fractured rock mass with correlated fracture length and aperture. Int J Rock Mech Min Sci 45(8):1320–1334

Bandis SC, Lumsden AC, Barton NR (1983) Fundamentals of rock joint deformation. Int J Rock Mech Min Sci Geomech Abstr 20(6):249–268

Choi DS, McCain DL (1980) Design of longwall systems. Trans Soc Min Eng AIME 268:1761–1764

Chuen LT (1979) Practice and knowledge of coal mining under water bodies. In: Proceeding of the 10th World Mining Congress, vol III, Istanbul, Turkey

Das SK (2000) Observations and classification of roof strata behaviour over longwall coal mining panels in India. Int J Rock Mech Min Sci 37(4):585–597

Fawcett RJ, Hibberd S, Singh RN (1986) Analytic calculations of hydraulic conductivities above longwall coal faces. Int J Min Water 5(1):45–60

Fransson Å, Tsang C, Rutqvist J et al (2010) Estimation of deformation and stiffness of fractures close to tunnels using data from single-hole hydraulic testing and grouting. Int J Rock Mech Min Sci 47(6):887–893

Guo GL, Miao XX, Zhang ZN (2002) Research on ruptured rock mass deformation characteristics of Longwall goafs. Sci Technol Eng 2:44–47 (In Chinese)

Hao S, Shuguang J, Lanyun W (2011) Bulking factor of the strata overlying the gob and a three-dimensional numerical simulation of the air leakage flow field. Min Sci Technol (China) 21:261–266

Hardin EL, Cheng CH, Paillet FL et al (1987) Fracture characterization by means of attenuation and generation of tube waves in fractured crystalline rock at Mirror Lake, New Hampshire. J Geophys Res: Solid Earth (1978–2012) 92 (B8):7989–8006

Karacan CÖ, Esterhuizen GS, Schatzel SJ et al (2007) Reservoir simulation-based modeling for characterizing longwall methane emissions and gob gas venthole production. Int J Coal Geol 71(2):225–245

Karacan CÖ, Goodman G (2009) Hydraulic conductivity changes and influencing factors in longwall overburden determined by slug tests in gob gas ventholes. Int J Rock Mech Min Sci 46(7):1162–1174

Kim J, Parizek RR, Elsworth D (1997) Evaluation of fully-coupled strata deformation and groundwater flow in response to longwall mining. Int J Rock Mech Min Sci 34(8):1187–1199

King HJ, Whittaker BN (1971) A review of current knowledge on roadway behaviour, especially the problems on which further information is required. In: Proceeding of the Symposium on Strata Control in Roadway (1970). IME, London, pp 73–90

Lee SD, Harrison JP (2001) Empirical parameters for non-linear fracture stiffness from numerical experiments of fracture closure. Int J Rock Mech Min Sci 38(5):721–727

Li T, Mei T, Sun X et al (2013) A study on a water-inrush incident at Laohutai coalmine. Int J Rock Mech Min Sci 59:151–159

Li HC, Wang QP, Quan YP (1992) A study on stress distribution and reasonable size of coal pillar in a coal face. In: Proceeding of 11th International Conference on Ground Control in Mining, pp 30–37

Liu J, Elsworth D (1997) Three-dimensional effects of hydraulic conductivity enhancement and desaturation around mined panels. Int J Rock Mech Min Sci 34(8):1139–1152

Liu J, Elsworth D, Brady BH (1999) Linking stress-dependent effective porosity and hydraulic conductivity fields to RMR. Int J Rock Mech Min Sci 36(5):581–596

Liu H, Rutqvist J, Berryman JG (2009) On the relationship between stress and elastic strain for porous and fractured rock. Int J Rock Mech Min Sci 46(2):289–296

Lubbe R, Worthington MH (2006) A field investigation of fracture compliance. Geophys Prospect 54(3):319–331

Majdi A, Hassani FP, Nasiri MY (2012) Prediction of the height of destressed zone above the mined panel roof in longwall coal mining. Int J Coal Geol 98:62–72

Mark C (1992) Analysis of longwall pillar stability (ALPS): an update. In: Iannacchione AT, Mark C, Repsher RC, Tuchman RJ, Simon CC (eds) Proceeding of the Workshop on Coal Pillar Mechanics and Design: US Department of the Interior, Bureau of Mines, IC. Pittsburgh 9315:238–249

Niskovskiy Y, Vasianovich A (1996) Investigation of possibility to apply untraditional and ecologically good methods of coal mining under sea bed. In: The 6th International Offshore and Polar Engineering Conference. International Society of Offshore and Polar Engineers, pp 51–53

Oda M (1986) An equivalent continuum model for coupled stress and fluid flow analysis in jointed rock masses. Water Resour Res 22(13):1845–1856

Pappas DM, Mark C (1993) Behavior of simulated longwall gob material. Report of Investigations No. 9458. US Dept. of Interior, US Bureau of Mines

Pariseau WG (1993) Equivalent properties of a jointed Biot material. Int J Rock Mech Min Sci Geomech Abstr 30(7):1151–1157

Peng SS, Chiang HS (1984) Longwall mining. John Wiley & Sons Inc, New York

Ren TX, Edwards JS, Jozefowicz RR (1997) CFD modeling of methane flow around longwall coal faces. In: 6th International Mine Ventilation Congress, pp 17–22

Salamon MDG (1990) Mechanism of caving in longwall coal mining. In: Rock Mechanical Contributions and Challenges: Proceeding of the 31st US Symposium. Golden, Colorado, pp 161–168

Schatzel SJ, Karacan CÖ, Dougherty H et al (2012) An analysis of reservoir conditions and responses in longwall panel overburden during mining and its effect on gob gas well performance. Eng Geol 127:65–74

Shabanimashcool M, Li CC (2012) Numerical modelling of longwall mining and stability analysis of the gates in a coal mine. Int J Rock Mech Min Sci 51:24–34

Singh MM, Kendorski FS (1981) Strata disturbance prediction for mining beneath surface water and waste impoundments. Proceeding of 1st conference on ground control in mining, Morgantown, pp 76–89

Singh R, Singh TN, Dhar BB (1995) Coal pillar loading in shallow mining conditions. Int J Rock Mech Min Sci Geomech Abstr 33(8):757–768

Steer P, Bigot A, Cattin R et al (2011) In-situ characterization of the effective elasticity of a fault zone, and its relationship to fracture spacing. J Struct Geol 33(11):1541–1553

Sui W, Hang Y, Ma L et al (2015) Interactions of overburden failure zones due to multiple-seam mining using longwall caving. Bull Eng Geol Environ 74:1019–1035

Sun Y, Xu Z, Dong Q et al (2008) Forecasting water disaster for a coal mine under the Xiaolangdi reservoir. J China Univ Min Technol 18(4):516–520

Theis CV (1935) The relation between the lowering of the piezometric surface and the rate and duration of discharge of a well using ground water storage. Transactions of the American Geophysical Union 16, 519–524

Wang WX, Sui WH, Dong QH et al (2013) Closure effect of mining-induced fractures under sand aquifers and prediction of overburden failure due to re-mining. J China Coal Soc 38(10):1723–1729 (In Chinese)

Wang WX, Sui WH, Dong QH et al (2014) Influence of cover stress re-establishment on the permeability evolution of the mining-induced fractures. J China Coal Soc 39(06):1031–1038 (In Chinese)

Worthington MH, Lubbe R (2007) The scaling of fracture compliance. Geol Soc London Spec Publ 270(1):73–82

Yavuz H (2004) An estimation method for cover pressure re-establishment distance and pressure distribution in the goaf of longwall coal mines. Int J Rock Mech Min Sci 41(2):193–205

Zhang D, Fan G, Liu Y et al (2010) Field trials of aquifer protection in longwall mining of shallow coal seams in China. Int J Rock Mech Min Sci 47(6):908–914

Zhang YJ, Kang YH, Liu XE (2006) Predicting on inrush of sand of mining under loosening sandstone aquifer. J China Coal Soc 31(4):429–432 (In Chinese)

Zhang J, Shen B (2004) Coal mining under aquifers in China: a case study. Int J Rock Mech Min Sci 41(4):629–639

Zhu W, Wang P (1993) Finite element analysis of jointed rock masses and engineering application. Int J Rock Mech Min Sci Geomech Abstr 30(5):537–544